QUARTERLY JOURNAL
OF THE
ROYAL METEOROLOGICAL SOCIETY

Vol. 124 APRIL 1998 Part B No. 548

Q. J. R. Meteorol. Soc. (1998), **124**, pp. 1019–1043

Storm-track organization and variability in a simplified atmospheric global circulation model

By THOMAS FRISIUS[1], FRANK LUNKEIT[1], KLAUS FRAEDRICH[1]* and IAN N. JAMES[2]
[1]*Universität Hamburg, Germany*
[2]*University of Reading, UK*

(Received 1 August 1996; revised 11 September 1997)

SUMMARY

A storm track is simulated in a coarse-resolution multilevel primitive-equation model with linear surface friction and heating terms. A restoration temperature distribution consisting of a dipole embedded in a zonally symmetric profile forces the model to simulate the surface heating. Three simulations, each with a different dipole orientation, are performed to test the sensitivity of storm-track organization to the external forcing field. The climatological time-mean circulation and the transient disturbances of the reference simulation agree well with observations of northern hemisphere wintertime storm tracks. Local energetics show that baroclinic instability is responsible for the enhanced eddy kinetic energy downstream of the jet, and the downstream end of the storm track results from the barotropic conversions of eddy kinetic energy to the time-mean flow.

Low-frequency fluctuations with a period of about 50 days associated with a retrograding large-scale wave pattern are identified by a complex empirical-orthogonal-function analysis of the vertically averaged stream function. A composite life cycle of the low-frequency variability reveals the growth and decay of a blocking anticyclone downstream of the storm track. A cyclogenesis initiated by an eastward-propagating wave train is observed a few days before the amplitude of the low-frequency anomaly attains its peak. The net forcing of the high-frequency eddies contributes to the growth and decay of the blocking anticyclone. The results suggest that the occurrence of the blocking-like event is part of the storm-track dynamics.

KEYWORDS: Blocking anticyclones Low-frequency variability Low-resolution model Storm life cycles

1. INTRODUCTION

A basic feature of the northern hemisphere atmospheric wintertime circulation is the concentration of the mid-latitude eddy activity in the so called North Atlantic and North Pacific storm tracks. The features of these storm tracks have been investigated by many observational studies (for example, Blackmon (1976), Blackmon *et al.* (1977) and Lau (1979a,b)). The physical mechanisms for the organization of storm tracks, however, remain less clear. There are two possible explanations for why storm tracks may persist: (a) the temperature gradients can be maintained by land–sea contrasts and are thus fixed by the lower boundary inducing planetary-scale stationary waves by heating, orographic effects or transients (Smagorinsky 1953; Held 1983; Hoskins and Valdes 1990; Ting 1994); and (b) the storm tracks organize themselves by the feedback of the eddies to the time-mean flow (Chang and Orlanski 1993). It was proposed by Pierrehumbert (1984) that the zonally varying flow of the northern hemisphere may lead to the growth of local modes which will have maximum amplitude downstream of the jets. It was indeed revealed by

* Corresponding author: Meteorologisches Institut der Universität Hamburg, Bundesstraße 55, D-20146 Hamburg, Germany.

Frederiksen (1983) that the fastest-growing linear modes of the observed climatological January flow are localized in the storm-track regions. But these approaches are based on linear theory without containing the feedback loop between mean flow and eddies. This includes the importance of a zonally asymmetric distribution of heating by the transients for the maintenance of zonally varying baroclinicity as discussed in a linear stationary response study of Hoskins and Valdes (1990).

The organization of storm tracks due to heating can only be investigated with non-linear models. Mole and James (1990) simulated a storm track in a global multilayer primitive-equation model which was driven by Newtonian cooling towards a target state consisting of a zonal wave-number one temperature perturbation. The results showed that heating can lead to localization of eddy activity. The simulated storm track had a wave-number one structure like the target state. Chang and Orlanski (1993) investigated the dynamics of storm tracks in a primitive-equation channel model. The zonally varying baroclinicity was forced with an artificial sponge region. This experimental set-up was motivated by the observation of transient temperature fluxes growing in amplitude during the first part of a wave life cycle. Their negative feedback on baroclinicity can thus be expected to occur downstream of a localized baroclinicity maximum. Their simulations reveal a downstream development of the eddies in the storm track by the ageostrophic geopotential fluxes, thus avoiding a localization of eddy energy. Only by enhancing dissipation in the downstream part of the channel were they able to terminate the downstream development. They concluded that zonally varying surface friction (weakened over the oceans and enhanced over the continents) is essential for the localization of the northern hemisphere storm tracks. Another storm-track simulation (Whittaker and Dole 1995) is based on a two-layer quasi-geostrophic channel model which was relaxed towards a zonally varying basic state. In contrast to the results of Chang and Orlanski (1993) they found a development of a well-defined storm track. Here the barotropic decay processes determine the location of the downstream end of the storm track. The differences between the results suggest that the organization of a storm track in the models depends on various model parameters that are not necessarily characteristic for the northern hemisphere wintertime circulation.

The variability of the observed northern hemisphere storm tracks has been analysed by Lau (1988) in terms of empirical orthogonal functions (EOFs) of the monthly mean fields of the bandpass filtered standard deviation of 500 hPa geopotential height. This study led to the result that the zonal displacements of the Pacific storm track dominate over the meridional displacements, whereas in the Atlantic storm track the opposite is the case. The correlations between the EOFs and the geopotential-height field reveal similarity to the teleconnection pattern identified by Wallace and Gutzler (1981), suggesting an interaction between high-frequency eddies of the storm track and low-frequency fluctuations. The most prominent example for such an interaction is the blocking event defined by the quasi-stationary appearance of an anticyclone over the eastern part of the oceans (Rex 1950). Several studies have found that blocking events are preceded by enhanced synoptic-scale variability in the upstream storm track (e.g. Colucci 1985; Dole 1986; Nakamura and Wallace 1990). Furthermore, a number of publications show that the blocking anticyclone is directly maintained by vorticity fluxes of the high-frequency eddies (e.g. Hoskins *et al.* 1983; Illari and Marshall 1983; Mullen 1987).

The motivation for the present paper is to analyse the organization and variability of a northern hemispheric type storm track depending on the zonally varying heating. This includes the interaction between high-frequency eddies and low-frequency fluctuations as a possible source for storm-track variability. For these purposes the global multilayer primitive-equation model (Mole and James 1990) is adopted. The model is driven by target

states representing idealized temperature contrasts. Three simulations are performed to test the sensitivity of the storm track to the external forcing. One of these states resembles the northern hemisphere temperature distribution in winter. The physical mechanisms for the storm-track organization are analysed in terms of transient eddy diagnostics and local energetics. The low-frequency fluctuations of the storm track are detected by a complex EOF analysis. Insight into the dynamical behaviour is gained by a composite life cycle of the low-frequency fluctuations constructed from the associated complex principal component time series. Model, experiment, and the simulated mean climatology are presented in section 2. In section 3 the transient eddy statistics and their local energetics are examined. The dynamics of the low-frequency fluctuations are analysed in section 4. A discussion of the results in section 5 closes the paper.

2. Model experiments and climatology

The global atmospheric primitive-equation model used in this study is based on the multilayer spectral model (Hoskins and Simmons 1975) solving the primitive equations on sigma levels with a semi-implicit time scheme. The model, previously introduced by James and Gray (1986) and used by Mole and James (1990), is a simplified global circulation model (SGCM) including linear Rayleigh friction and Newtonian cooling to represent dissipative and diabatic processes, respectively. The SGCM is further adopted by James and James (1992) and James *et al.* (1994) for analysing low-frequency anomalies in a zonally symmetric flow. For the present simulation the model is hemispheric with T21 (ca. 5.6° × 5.6°) horizontal resolution and five equally spaced sigma levels in the vertical. Orography and moisture are not included. The model consists of the following prognostic equations:

$$\frac{\partial \eta}{\partial t} = -\mathbf{k} \cdot \nabla \times \left(\eta \mathbf{k} \times \mathbf{v} + \dot{\sigma} \frac{\partial \mathbf{v}}{\partial \sigma} + RT \nabla \ln p_s \right) - \frac{\eta - f}{\tau_F} + K \nabla^8 (\eta - f), \quad (1)$$

$$\frac{\partial D}{\partial t} = -\nabla \cdot \left(\eta \mathbf{k} \times \mathbf{v} + \dot{\sigma} \frac{\partial \mathbf{v}}{\partial \sigma} + RT \nabla \ln p_s \right) - \nabla^2 \left(\frac{1}{2} \mathbf{v} \cdot \mathbf{v} + \phi \right) - \frac{D}{\tau_F} + K \nabla^8 D, \quad (2)$$

$$\frac{\partial T}{\partial t} = -\mathbf{v} \cdot \nabla T - \dot{\sigma} \frac{\partial T}{\partial \sigma} + \frac{RT}{c_p} \frac{\omega}{p} + \frac{T_E - T}{\tau_E} + K \nabla^8 T, \quad (3)$$

$$\frac{\partial (\ln p_s)}{\partial t} = -\hat{\mathbf{v}} \cdot \nabla \ln p_s - \hat{D}, \quad (4)$$

where $\mathbf{v} = (u, v)$ is the horizontal wind vector, η the absolute vorticity, f the Coriolis parameter, D the horizontal divergence, T the temperature, ϕ the geopotential, p the pressure, p_s the surface pressure, $\sigma = p/p_s$ the vertical coordinate, $\dot{\sigma}$ the vertical sigma velocity, ω the vertical pressure velocity, R the gas constant, c_p the specific heat capacity at constant pressure and t the time; $\mathbf{k}$ denotes the unit vector normal to the sphere, ∇ the horizontal gradient operator and $\hat{(\ )}$ the vertical averaging operator; τ_E and τ_F represent the constant relaxation times for Newtonian cooling and Rayleigh friction, respectively. The restoration temperature, to which the temperature will be relaxed, is given by T_E. K is the coefficient for the eighth-order hyperdiffusion which is determined so that a wave of total wave number 21 is damped with a time-scale of 0.25 days. The model is completed by diagnostic equations for $\mathbf{v}$, $\dot{\sigma}$, ω and ϕ;

$$\mathbf{v} = \mathbf{k} \times \nabla(\nabla^{-2}(\eta - f)) + \nabla(\nabla^{-2} D), \quad (5)$$

$$\dot{\sigma} = -\int_0^\sigma (D - \hat{D})\, d\sigma - \int_0^\sigma (\mathbf{v} - \hat{\mathbf{v}}) \cdot \nabla \ln p_s \, d\sigma, \quad (6)$$

TABLE 1. EXPERIMENTAL DESIGN

Experiment	Orientation of isotherms	Display
NE	North-east	Fig. 1(a)
Z	Zonal	Fig. 1(b)
SE	South-east	Fig. 1(c)

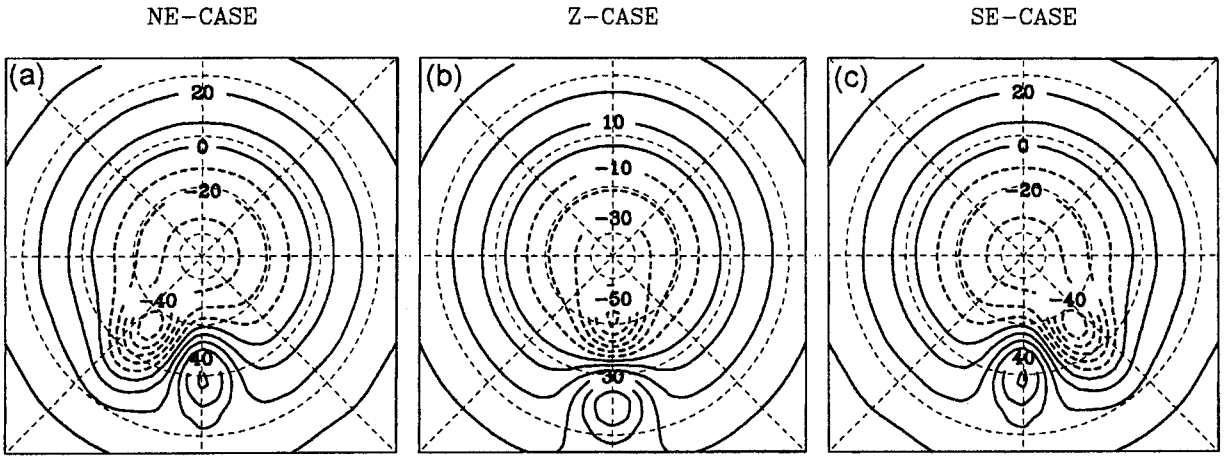

Figure 1. Restoration temperature at $\sigma = 0.9$ for (a) the NE-case, (b) the Z-case, and (c) the SE-case. The contour interval is 10 degC and negative isolines are shown dashed.

$$\omega = p\left(\frac{\dot{\sigma}}{\sigma} + (\mathbf{v} - \widehat{\mathbf{v}}) \cdot \nabla \ln p_s - \widehat{D}\right), \tag{7}$$

$$\frac{\partial \phi}{\partial(\ln \sigma)} = -RT, \tag{8}$$

where the ∇^{-2} operator is evaluated by considering the periodic boundary conditions of the sphere.

For the storm-track simulation, the T_E distribution requires a zonally varying temperature gradient which is introduced by a temperature dipole superimposed on a zonally symmetric temperature profile. The simulations discussed here are run in hemispheric mode. Additional global simulations are performed, omitting the temperature dipole of the restoration temperature in the southern hemisphere. The results show that the potential reflection of waves at the equator can be neglected for the simulated mid-latitude storm-track dynamics. Three experiments with different dipole orientations are performed (see Table 1); Fig. 1 (a polar stereographic projection with latitude circles at 20°N, 40°N, 60°N and 80°N is used in Fig. 1 and other similar figures) displays the horizontal T_E distributions at the lowest model layer, $\sigma = 0.9$. Note that the NE-case corresponds to the surface temperature distribution in northern hemispheric winter; the Z-case shows some similarities with summer conditions whereas the SE-case is somewhat artificial. The mathematical formula for the dipole structure is given in the appendix. In a vertical direction the amplitude of the temperature anomalies decreases to zero, avoiding a blow up of the zonal wind at the top model layer. Here it should be noted that due to the temperature advection T_E cannot be interpreted as a climatologically averaged equilibrium temperature $\bar{T}$: in the time-mean, the Newtonian cooling term (representing the total diabatic warming of the order of 5 K day^{-1} at 900 hPa) balances the nonlinear temperature advection. Thus, a large temperature contrast between T_E and $\bar{T}$ (about 25 K) is to be expected if the relaxation time-scale (5 days) is large.

The global mean tropospheric vertical temperature gradient of the target state amounts to -6.5 K km^{-1}. The magnitude of the vertical temperature gradient is increased over the warm anomalies (at $\sigma = 0.7$: -9.36 K km^{-1} for the NE-case and SE-case, and -9.716 K km^{-1} for the Z-case) and reduced over the cold anomalies (at $\sigma = 0.7$: -0.545 K km^{-1} for the NE-case and SE-case, and 0.061 K km^{-1} for the Z-case). Due to the stable stratification the model does not require convective adjustment. A tropopause is introduced at 12 km height above which the vertical temperature gradient vanishes. This reduces the vertical temperature gradient between the upper two levels given by the vertical resolution. The time constant for Newtonian cooling τ_E varies vertically to account for the height dependence of the heat exchange with faster exchange in the lower layers: τ_E is 5 days at $\sigma = 0.9$, 10 days at $\sigma = 0.7$, and 30 days elsewhere. The time-scales chosen are comparable with Held and Suarez (1994) and James (1994): the Newtonian cooling rate in the upper layers corresponds to the longer radiative time-scales, while the shorter time-scales in the lower levels characterize the turbulent heat-exchange processes with the underlying surface. One of the major drawbacks of Newtonian cooling related to storm-track simulation is the use of constant relaxation times which do not adequately describe, for example, the latent-heat release in the transient eddies. Rayleigh friction is introduced only at the bottom layer, with a time constant $\tau_F = 1$ day. A vertical diffusion is not applied in the model. The experiments are run for 110 years. The time averaging to derive the climatologies refers to the period from year 11 to year 110 of the simulations. The first ten years are deleted although the spin-up period is only about one year.

The climatologies of the time-mean circulation are presented for selected horizontal fields (Fig. 2): the horizontal distributions of the temperature at 900 hPa, the vertical integral of heating, the surface pressure and the meridional wind at 300 hPa. In all three experiments the temperature field at 900 hPa (Fig. 2(a)) is dominated by the zonal asymmetries of T_E. The direction of the temperature isolines in the region of the largest temperature gradients is determined by the orientation of the T_E–temperature dipole. The temperature differences between the cold and warm anomalies are considerably smaller than in the target state (about 50% reduction). In view of the Newtonian cooling formulation, the strongest values of heating and cooling occur near the warm and cold spots of the target states (Fig. 2(b)). The vertical heating profile decreases strongly with height: maximum values are 10 K day^{-1} (900 hPa), 4 K day^{-1} (700 hPa) and 0.5 K day^{-1} (500 hPa). These magnitudes are about a factor 2 larger than the values presented by Valdes and Hoskins (1989, Fig. 2) which, however, is considered reasonable for the idealized experimental design. The heating obviously acts to maintain the zonally varying baroclinicity against the divergence of transient and stationary temperature fluxes. This suggests that the organization of the storm tracks analysed in the present paper result from the zonally asymmetric heating distribution.

The surface pressure distribution (Fig. 2(c)) shows a stationary high-pressure centre near the cooling anomaly in all three cases. In the NE-case and the Z-case a stationary low-pressure centre occurs downstream at a higher latitude. In contrast, the low-pressure centre of the SE-case is found upstream of the cold anomaly. The surface pressure distribution of the NE-case and the Z-case is comparable with the oceanic low and continental high pressure cells observed in the northern hemisphere wintertime circulation (Blackmon *et al.* 1977), whereas the SE-case is not. The meridional wind field at 300 hPa (Fig. 2(d)) reveals in all three cases a stationary wave pattern with largest amplitude near the heating anomalies. Cyclonic (anticyclonic) shear of meridional wind is detected near the cold (warm) anomaly at the surface. This is in agreement with the theoretical model of Smagorinsky (1953), who investigated the effect of large-scale heat sources on the stationary circulation. Further downstream the stationary wave is radiated towards the south-east. The zonally

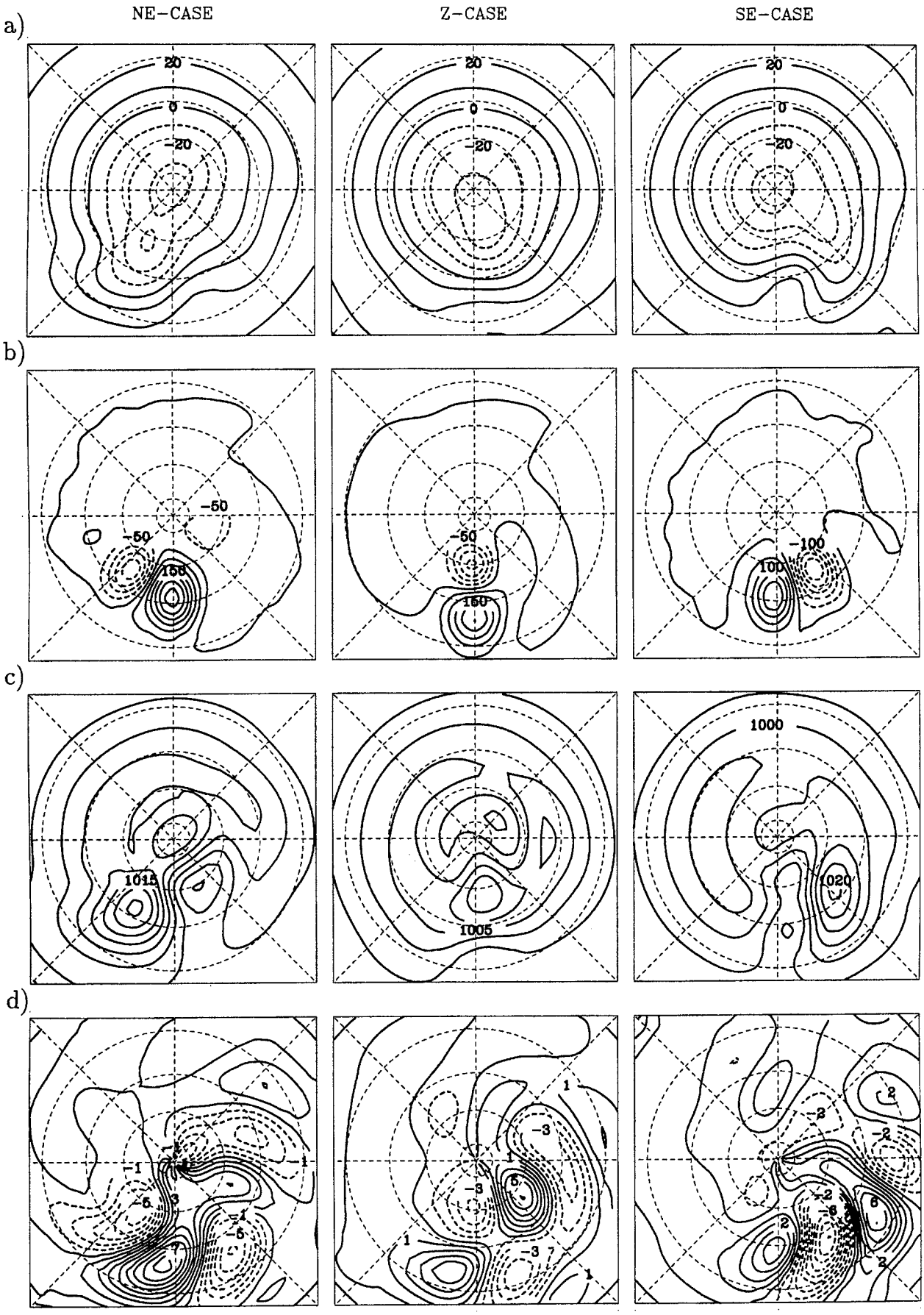

Figure 2. Time-mean quantities for the NE-case (left column), the Z-case (middle column) and the SE-case (right column): row (a) temperature at 900 hPa (contour interval 10 degC), row (b) vertical integral of heating (contour interval 50 W m^{-2}), row (c) surface pressure (contour interval 5 hPa), and row (d) meridional wind at 300 hPa (contour interval 1 m s^{-1}). Negative isolines are shown dashed.

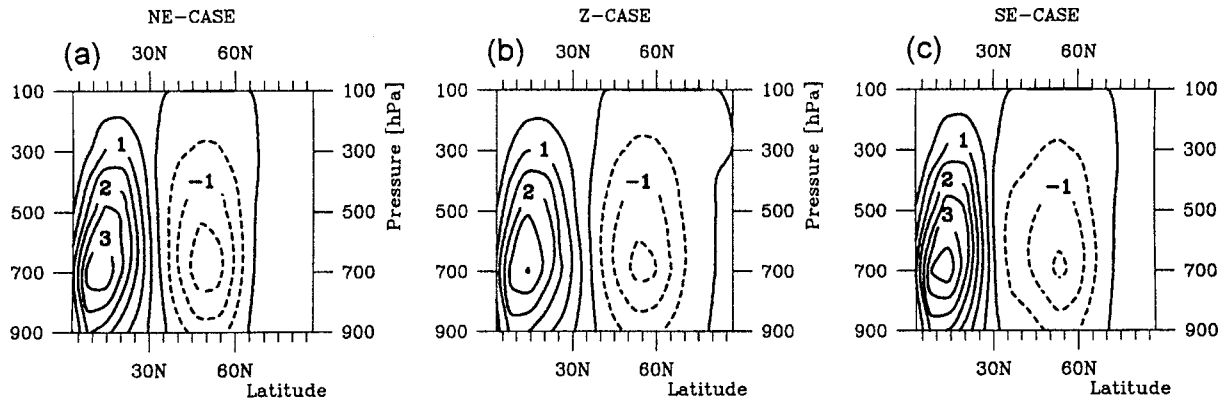

Figure 3. Mass stream function of the zonally averaged time-mean meridional circulation for (a) the NE-case, (b) the Z-case, and (c) the SE-case. The contour interval is 0.5×10^{10} kg s^{-1} and negative isolines are shown dashed.

averaged meridional circulation is represented in terms of the mass stream function (Fig. 3). For all cases the model reproduces the position and magnitude of the Hadley and Ferrel cells reasonably well.

3. Storm-track analysis: transient eddies and local energetics

Transient eddy statistics, which include the three-dimensional pseudo **E**-vector and local energetics, are applied to analyse the dynamical properties of the storm track before low-frequency variability of the storm track is discussed.

(*a*) *Transient eddies*

A bandpass filter introduced by Trenberth (1991) is used to extract the high-frequency eddy variability. The filter retains periods between 2 and 8 days using 15 weights; its width exceeds the Blackmon bandpass filter (Blackmon 1976) which is based on 31 weights by about a day or two. It should be mentioned that applying bandpass filtering could result in spurious storm-track intensities simply due to zonally asymmetric eddy propagation speeds. A Hovmüller diagram of the NE-case (Fig. 4) for the unfiltered meridional wind anomaly at 300 hPa (averaged from 40°N to 60°N) shows this not to be the case. The waves propagate around the globe with roughly constant phase speed and enhanced amplitudes in the storm-track region. This feature is not affected by bandpass filtering.

As mentioned in the introduction, the zonal variation of the baroclinicity of the mean circulation is a crucial factor for localizing eddy activity. An appropriate measure of baroclinicity is the maximum growth rate of the Eady wave (Eady 1949, see also Lindzen and Farrel (1980)):

$$\sigma_{\mathrm{BI}} = 0.31 \frac{f}{N} \frac{\partial |\mathbf{v}|}{\partial z}, \tag{9}$$

where N denotes the Brunt–Väisälä frequency and z the geopotential height. This measure has also been applied by, for example, Hoskins and Valdes (1990), Chang and Orlanski (1993), Hall *et al.* (1994) and Lunkeit *et al.* (1996). In these studies the maximum geopotential-height variance is observed downstream of the σ_{BI} maximum. This relationship between time-mean baroclinicity and eddy activity is displayed in Fig. 5, showing the baroclinicity parameter σ_{BI} at 700 hPa and the bandpass filtered standard deviation of geopotential height at 500 hPa for the three experiments. All distributions of σ_{BI} (Fig. 5(a)) are similar to those of the zonal wind at 300 hPa, indicating that the upper-level winds

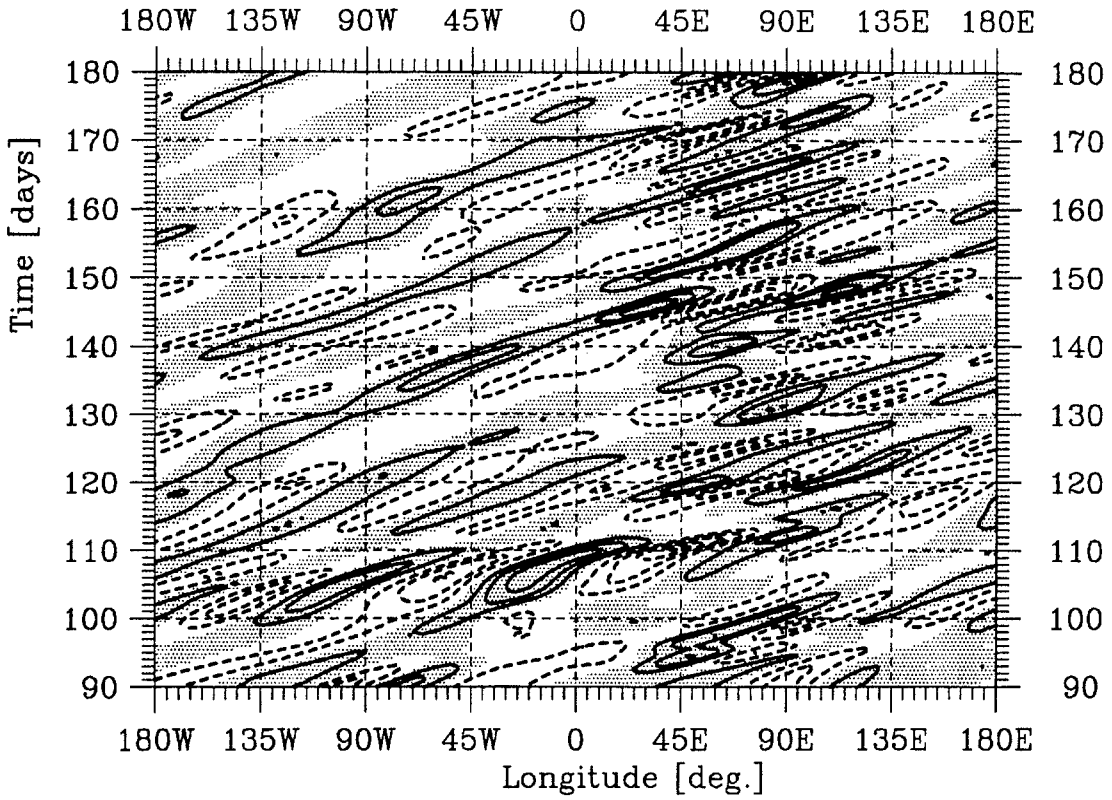

Figure 4. Hovmüller diagram for the unfiltered meridional velocity anomaly at 300 hPa meridionally averaged from 40°N to 60°N (contour interval 5 m s^{-1}). Positive values are shaded, negative isolines are dashed, and the zero line is not displayed.

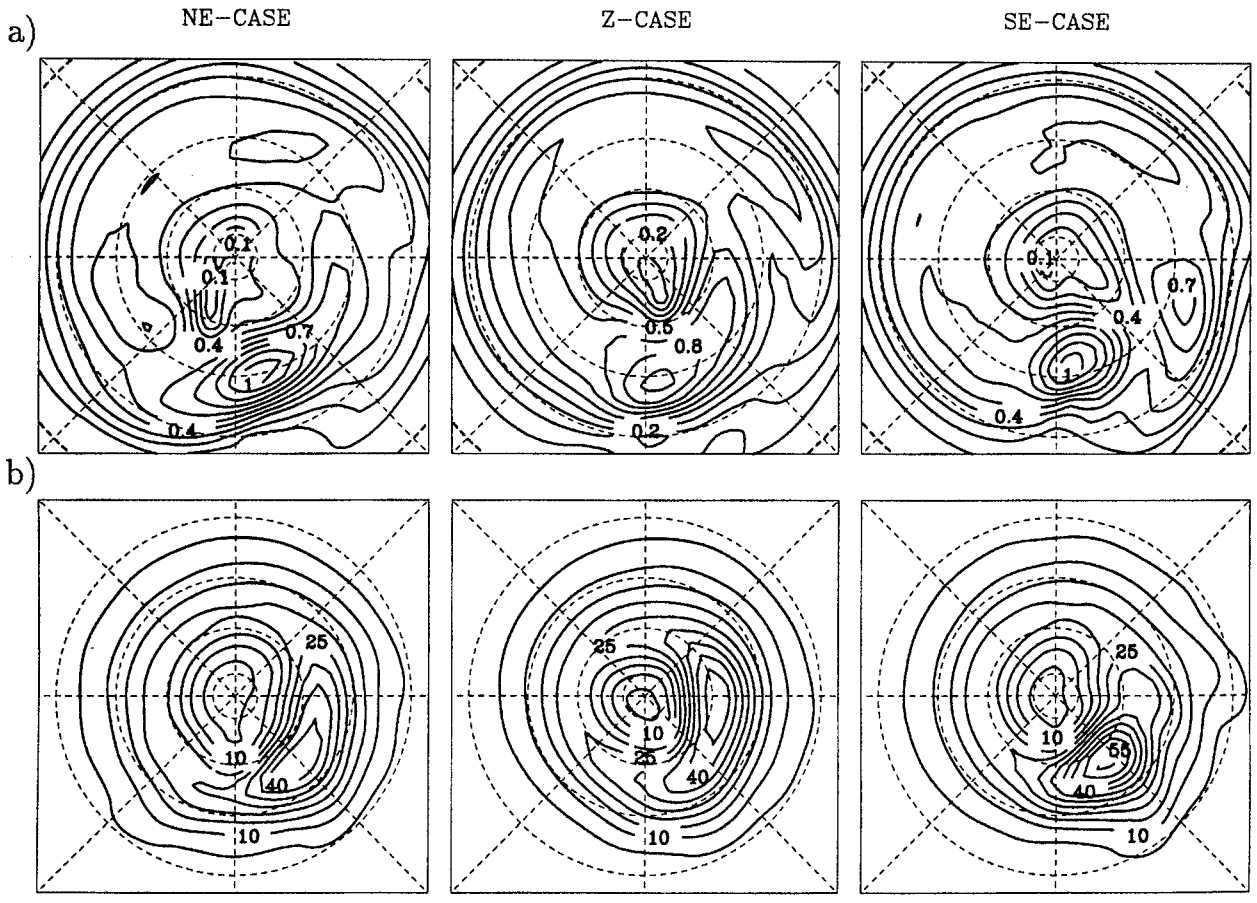

Figure 5. Row (a) baroclinicity parameter at 700 hPa (contour interval 0.1 day^{-1}), and row (b) bandpass filtered standard deviation of geopotential height at 500 hPa (contour interval 5 m). Shown are the NE-case (left column), the Z-case (middle column), and the SE-case (right column).

are dominated by the thermal wind for all cases. Therefore, their anomaly patterns correspond to the thermal gradients induced by the dipole orientation. The sum of both thermal wind components comprises the baroclinicity σ_{BI}. For lower levels, the magnitude of $\sigma_{BI} \approx 1$ day^{-1} is comparable with data and model simulations (e.g. Hoskins and Valdes 1990; Lunkeit *et al.* 1996), whereas the upper level shows relatively low values. In the NE-case and the Z-case the region of enhanced baroclinicity extends over a considerable distance downstream, whereas in the SE-case this region has a small zonal extent. A secondary baroclinicity maximum is found downstream at a lower latitude. It stems from the surrounding low values; the negative eddy feedback reduces baroclinicity by temperature fluxes generating low values surrounding the secondary maximum of baroclinicity. The region of increased standard deviation (Fig. 5(b)) occurs downstream and northward of the jet for all cases. This is also a feature of the observed northern hemisphere storm tracks (Hoskins and Valdes 1990). The position of maximum standard deviation depends on the dipole orientation. In the Z-case the storm track is located farthest downstream, and in the SE-case farthest upstream. The SE-case shows a storm track with a small zonal extent, suggesting that the high-pressure system suppresses the transient disturbances. Damping by wave-phase-dependent cooling/heating, however, may not be the most favourable mechanism due to the large values of the geopotential height standard deviation (Fig. 5(b)). In all cases the magnitude of the standard deviation is reduced to 3/4 of the observed values (Blackmon 1976). The lack of latent-heat release in the waves is certainly one of the major causes of the relatively low standard deviations.

Another comprehensive diagnostic tool to describe the transient eddies in a storm track is the three-dimensional pseudo **E**-vector introduced by Hoskins *et al.* (1983):

$$\mathbf{E} = \left(\overline{v'^2 - u'^2},\ -\overline{u'v'},\ \frac{f}{\partial\bar{\theta}/\partial p}\overline{v'\theta'} \right), \tag{10}$$

where $\overline{(\,)}$ and $(\,)'$ denote the time average and its deviation, and θ is the potential temperature. **E** describes the propagation of transient wave activity relative to the time-mean flow. Figure 6 displays the horizontal components of **E** at 300 hPa (arrows) and the vertical component of **E** at 700 hPa (isolines) for the three cases. All cases reveal qualitatively similar distributions of **E** with the exception of the geographical location and zonal extent of the storm-track region. The propagation of wave activity is predominantly upward in the upstream part of the storm track due to the baroclinic conversions of the growing baroclinic waves. The horizontal propagation of wave activity is largest in the middle and downstream part. The meridional component of **E** increases towards the eastern end of the storm track, appearing as a spread of the vectors where the equatorward tilt is more dominant. The meridional propagation reflects the decay processes of the baroclinic disturbances. A similar distribution of **E** in the northern hemisphere storm tracks is observed by Hoskins *et al.* (1983). In summary, distributions of the transient eddies and mean circulation of the NE-case are most similar to the observations, although the magnitude of eddy activity is too weak. Only the NE-case is considered in the subsequent sections.

(*b*) *Local energetics*

The time-mean balance equation for transient kinetic energy $K_t = \frac{1}{2}(u'^2 + v'^2)$ supports the understanding of the physical processes of the localization of eddy energy. This

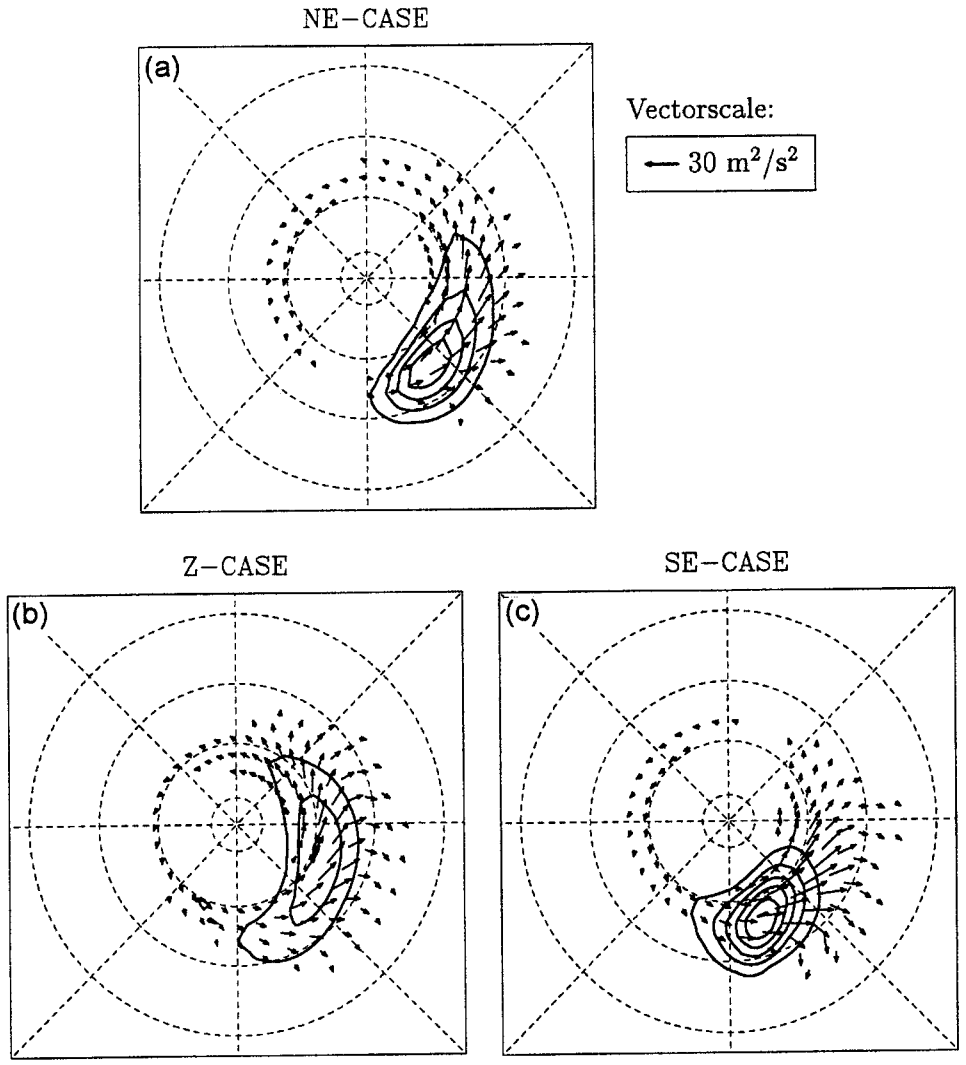

Figure 6. Bandpass filtered three-dimensional pseudo **E**-vector for (a) the NE-case, (b) the Z-case and (c) the SE-case: Horizontal components at 300 hPa (arrows) and vertical component at 700 hPa (isolines, contour interval 0.5 Pa m s^{-2}).

equation may be written in σ-coordinates (following Lau (1979a)):

$$
\begin{aligned}
0 = & -\bar{\mathbf{v}} \cdot \nabla \bar{K}_t - \bar{\dot{\sigma}} \frac{\partial}{\partial \sigma} \bar{K}_t && \Big\} \text{A} \\
& -\overline{\mathbf{v}' \cdot \nabla K_t} - \overline{\dot{\sigma}' \frac{\partial}{\partial \sigma} K_t} && \Big\} \text{B} \\
& -\overline{u'\mathbf{v}'} \cdot \nabla \bar{u} - \overline{v'\mathbf{v}'} \cdot \nabla \bar{v} - \overline{\dot{\sigma}'\mathbf{v}'} \cdot \frac{\partial \bar{\mathbf{v}}}{\partial \sigma} - (\bar{u}\overline{u'v'} - \bar{v}\overline{u'u'}) \frac{\tan \varphi}{a} && \Big\} \text{C} \\
& + f\mathbf{k} \cdot (\overline{\mathbf{v}' \times \mathbf{v}'_a}) && \} \text{D} \\
& -\frac{2\bar{K}_t}{\tau_F} && \Big\} \text{E} \\
& + \delta && \} \text{F},
\end{aligned}
\tag{11}
$$

where φ denotes the latitude and a the earth radius; the subscript 'a' refers to the ageostrophic wind. Lau (1979a) calculated the individual terms of this equation for observational data.

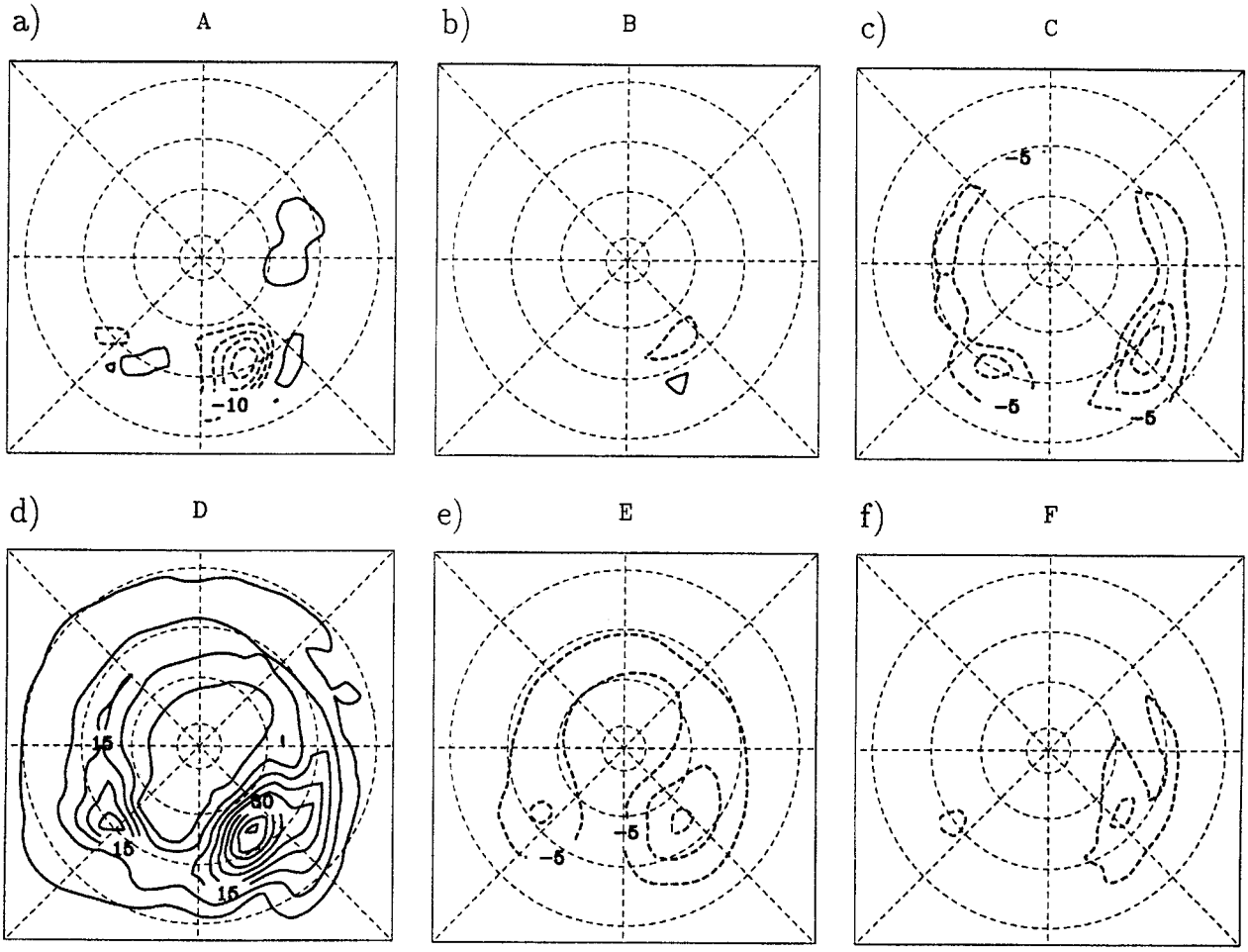

Figure 7. Energy balance for the NE-case (averaged over the four layers representing the troposphere): (a) advection of K_t by time-mean flow (term A), (b) advection of K_t by transient flow (term B), (c) shear production (destruction) (term C), (d) work by transient cross-isobaric flow (term D), (e) dissipation (term E), and (f) residual (term F). The contour interval is 5 J kg^{-1}day^{-1}, negative isolines are dashed and the zero line is not displayed. All terms are from Eq. (11).

The nonzero residual of the local energetics (term F) appears due to numerical effects (horizontal spectral scheme, time differencing) and dissipation by the hyperdiffusion. The terms of (11) are calculated from the unfiltered data of the NE-simulation and vertically averaged. From now on the vertical averages extend only over the four lowest layers representing the troposphere. Figure 7 displays the vertically averaged energy balance terms. The advection of transient kinetic energy by the time-mean flow (Fig. 7(a)) is characterized by a minimum upstream of the storm track and a weaker maximum downstream. This distribution is mainly a consequence of the advection by the time-mean zonal flow. The advection of transient kinetic energy by the transient flow (Fig. 7(b)) is small compared with term A. It mainly acts to diffuse the localized eddy kinetic energy. The shear production (destruction) (Fig. 7(c)) reveals only negative values. The global average of term C is identical to the conversion of transient kinetic energy to stationary kinetic energy. Therefore, the shear of the time-mean flow extracts energy from the transient eddies which is consistent with the observed global energy cycle (Lorenz 1955). In the south-eastern part of the storm track the shear destruction is enhanced. This suggests that the termination of eddy energy in the downstream part of the storm track is caused by barotropic processes. The shear of the meridional wind as well as the shear of the zonal wind contributes with the same magnitude to the total shear production (destruction). The work by transient cross-isobaric flow (Fig. 7(d)) has increased positive values in a band around 45°N. A large

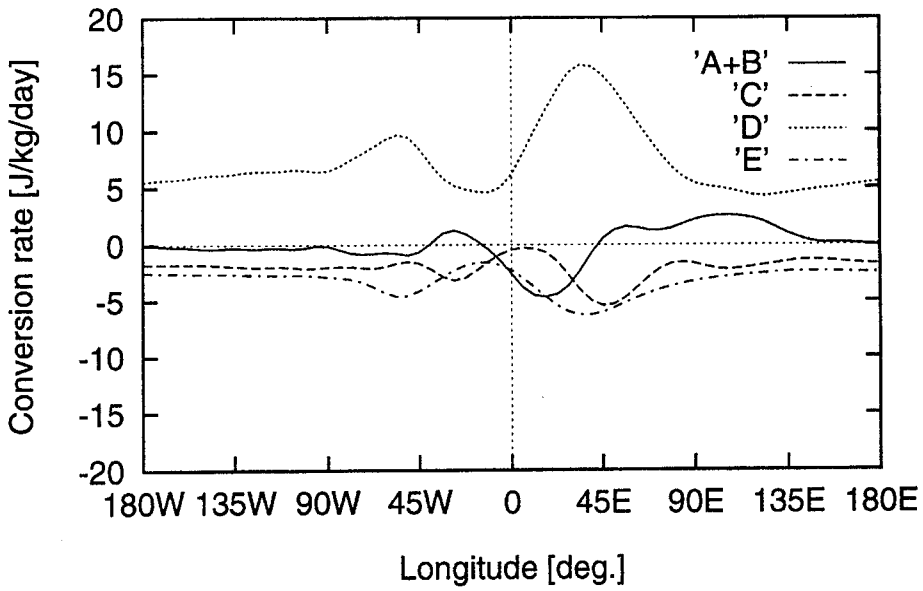

Figure 8. Vertically and meridionally averaged energy balance: advection of K_t (term A + B), shear production (destruction) (term C), work by transient cross-isobaric flow (term D), and dissipation (term E). All terms are from Eq. (11).

maximum is found in the upstream part of the storm track. Term D comprises the baroclinic production with only small contributions by the barotropic flow. Since the global average of the baroclinic production is identical to the conversion of transient available potential energy to transient kinetic energy, the kinetic energy in the storm track seems to result from baroclinic instability, which is also consistent with the observed global energy cycle. The dissipation (Fig. 7(e)) is proportional to the eddy kinetic energy in the lowest layer due to the formulation of Rayleigh friction. The negative residual (Fig. 7(f)) shows the transient kinetic energy is lost by numerical effects and hyperdiffusion. In the downstream part of the storm track enhanced values of this residual are found around 40°N which is most evident at the $\sigma = 0.3$ level (not shown). The large meridional convergence of the pseudo **E**-vector at this latitude (Fig. 6(a)) suggests that wave activity is dissipated by critical-layer absorption accompanied with a cascade to high wave numbers. This explains the increased subgrid-scale mixing parametrized by hyperdiffusion. This interpretation is consistent with the life-cycle simulations of MacVean (1983) and the energy-budget analysis of Stephenson (1994).

Figure 8 shows the energy-balance terms of Eq. (11) in the meridional and vertical average as functions of longitude. The only dominant positive contribution to the production of eddy energy in the storm-track region is given by the baroclinic production (term D). The advection is negative upstream and positive downstream of the storm track. Shear production (destruction) and dissipation act to decrease the eddy kinetic energy.

In a zonally symmetric flow the baroclinic wave life cycles are characterized by positive baroclinic conversions in the growth phase and negative barotropic conversions in the decay phase (Simmons and Hoskins 1978). Assuming a slowly varying zonal flow, a wave packet moving with a constant phase speed along the storm track would undergo a similar life cycle. The energy conversions of the wave packet as a function of longitude would be equivalent to the conversions as a function of time. The storm track appears as a cumulative effect of growing and decaying wave packets. Therefore Fig. 8 suggests that wave packets of the storm track behave like baroclinic waves in a zonally symmetric flow. However, the assumption of a slowly varying zonal flow is hardly justified since the baroclinic jet and the transient eddies have zonal scales of the same order.

4. Low-frequency fluctuations

As demonstrated in the foregoing sections, all three experiments show remarkable differences in the spatial and temporal characteristics, for example, of the stationary wave pattern and of the storm-track variability. One particular feature, only present in the NE-case, is low-frequency variability superimposed on the high-frequency fluctuations of the eddies. An EOF analysis of the vertically averaged stream function $\hat{\psi} = \nabla^{-2}(\hat{\eta} - f)$ shows that the first two EOFs describe a retrograding low-frequency wave pattern. A more powerful tool to isolate such propagating anomalies is given by complex EOF (CEOF) analysis. This method has also been applied by Kushnir (1987) to analyse retrograding (upstream propagating) low-frequency anomalies in the northern Pacific, and by Lanzante (1990) to identify the leading modes of 10–30 day variability. The method is only briefly described here (for more details see Horel (1984)). The analysed data set $\mathbf{z}(t)$ is given by the time series of the spectral coefficients of $\hat{\psi}$. These time series consist of daily data from year 11 to year 110 of the simulation. Both low-pass and unfiltered time data sets are being analysed. As the low-pass filtering does not essentially affect the analysis, only the unfiltered results are presented and discussed in the following.

The Hilbert transform $\tilde{\mathbf{z}}(t)$ of the data set has to be calculated for the analysis. For this purpose the time series, divided into ten subsets, are transformed by a fast Fourier transform into the spectral space where their phases are advanced by $\pi/2$, and then transformed back into the time space. A complex field is generated by

$$\mathbf{Z}(t) = \mathbf{z}(t) + \mathrm{i}\tilde{\mathbf{z}}(t), \tag{12}$$

where $\mathrm{i} = (-1)^{\frac{1}{2}}$.

The orthogonal complex eigenvectors $\mathbf{E}_n$ of the Hermitian covariance matrix of $\mathbf{Z}$ form the CEOF patterns of the analysis. The projection of the data field $\mathbf{Z}$ onto the CEOFs is written

$$\mathbf{Z}(t) = \sum_n P_n(t)\mathbf{E}_n, \tag{13}$$

where $P_n(t)$ is the nth complex principal component (CPC). From the orthogonality of $\mathbf{E}_n$, $P_n(t)$ can be calculated by

$$P_n(t) = \mathbf{Z}^*(t) \cdot \mathbf{E}_n, \tag{14}$$

where an asterisk denotes the complex conjugate. $A(t) = (P_n(t)P_n^*(t))^{\frac{1}{2}}$ represents the amplitude, and $\alpha = \tan^{-1}(\mathrm{Im}(P_n)/\mathrm{Re}(P_n))$ the phase of the corresponding CEOF pattern. To avoid ambiguity the phase is defined as the angle between the CPC and the negative real axis.

Figure 9 shows the pattern of CEOF-1 explaining 20% of the total variance. The real part of CEOF-1 (Fig. 9(a)) and the imaginary part of CEOF-1 (Fig. 9(b)) are similar to the EOF-1 and EOF-2 of the real EOF analysis (not shown). The real part of CEOF-1 (Fig. 9(a)) is dominated by a wave-like structure of three alternating extrema in the zonal direction, associated with a cyclonic perturbation in the storm-track region. The imaginary part of CEOF-1 (Fig. 9(b)) has a similar wave-like structure, but it is shifted eastward. Scanning along the 50°N latitude circle the observed rotation of the phase vectors (Fig. 9(c)) implies a zonal wave-number 1 disturbance propagating in the zonal direction.

A variance spectrum of the amplitude $A(t)$ of CPC-1 is displayed in Fig. 10(a). The spectrum is obtained by applying Bartlett's procedure with ten subsets of the time series. For comparison, the spectrum of an equivalent red-noise (first-order autoregressive) process and the 99% confidence limits for accepting a red-noise null hypothesis are calculated for periods longer than 5 days. The spectrum exhibits a broad maximum at a period of

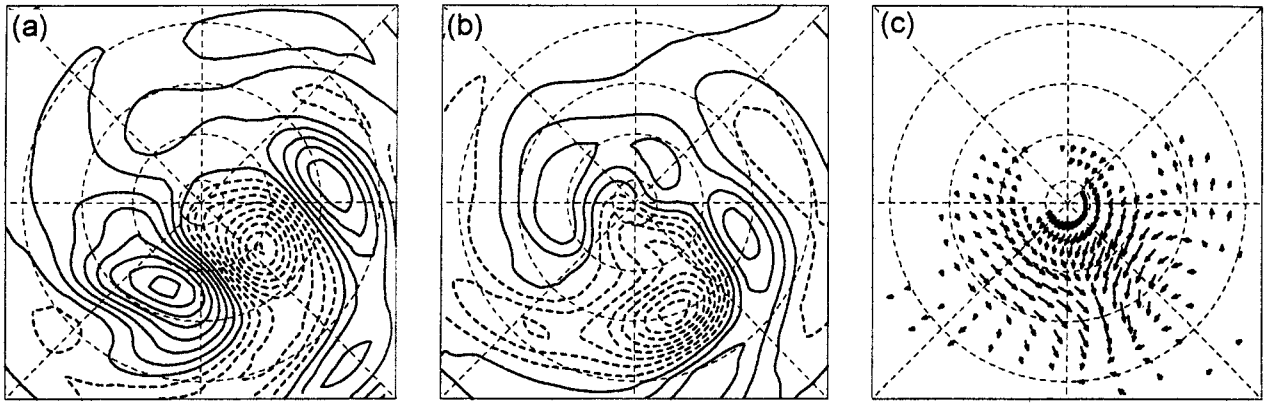

Figure 9. CEOF-1 pattern (see text) of the vertically averaged stream function: (a) real part, (b) imaginary part, and (c) vectorial representation. The length and orientation indicate magnitude and relative phase. Negative isolines are dashed.

50 days which is significant at the 99% level. This result suggests that CEOF-1 describes a low-frequency anomaly which undergoes a life cycle with a period of about 50 days. The time series of the amplitude and phase of CPC-1 in year 11 of the simulation are shown in Fig. 10(b) and Fig. 10(c), respectively. The time series of the amplitude confirms that the typical period of the amplitude variation is about 50 days. With the exception of high-frequency noise the phase increases with time. From the CEOF-1 pattern (Fig. 9) it becomes clear that this phase tendency corresponds to an upstream propagation of the anomaly.

More insight into the dynamics of the low-frequency fluctuations can be obtained by compositing their life cycles. The construction of the composites follows closely the procedure described by Kushnir (1987). For this purpose 47 maxima in the CPC-1 amplitude time series between year 11 and 20, which represent the mature stage of the life cycle, are identified. The interval between two successive maxima is required to exceed 50 days to neglect secondary maxima. If the interval between two maxima falls below 50 days then the smaller maximum is discarded. In Fig. 10(b) these maxima are marked by a square symbol. Figure 11 displays the selected maxima in the complex plane of CPC-1. No maxima are found when either the real or imaginary part is larger than zero. This corresponds to a state where a quasi-stationary cyclonic anomaly occurs in the downstream part of the storm track. Most maxima are detected when the opposite is the case. The CPC-1 composite of any variable G is now defined by

$$G_c(\tau) = (1/M) \sum_{k=1}^{M} G(t_k + \tau), \quad \tau = -20, \ldots, +20 \text{ days}, \tag{15}$$

where the index k denotes the kth maximum and M is the total number of identified maxima; the time lag τ describes the time evolution of CPC-1.

Figure 12 displays the composite of the amplitude A and phase α. As expected the amplitude grows and decays with maximum amplitude at day 0. The phase increases monotonically with time. At day 0 the positive phase is related to the occurrence of an anticyclonic anomaly at the eastern end of the storm track. Therefore, the time of maximum CPC-1 represents a blocking-like event. The $\hat{\psi}$-composite anomalies after subtracting the climatological mean show the growth and decay of the upstream propagating anticyclonic anomaly at day -10, day -5, day 0, day 5 and day 10 (Fig. 13). The significance calculated by a Student's t-test (shading in Fig. 13) indicates that the anomaly is statistically significant at the 99% level. The analysis of the ψ-composite anomalies at different pressure levels

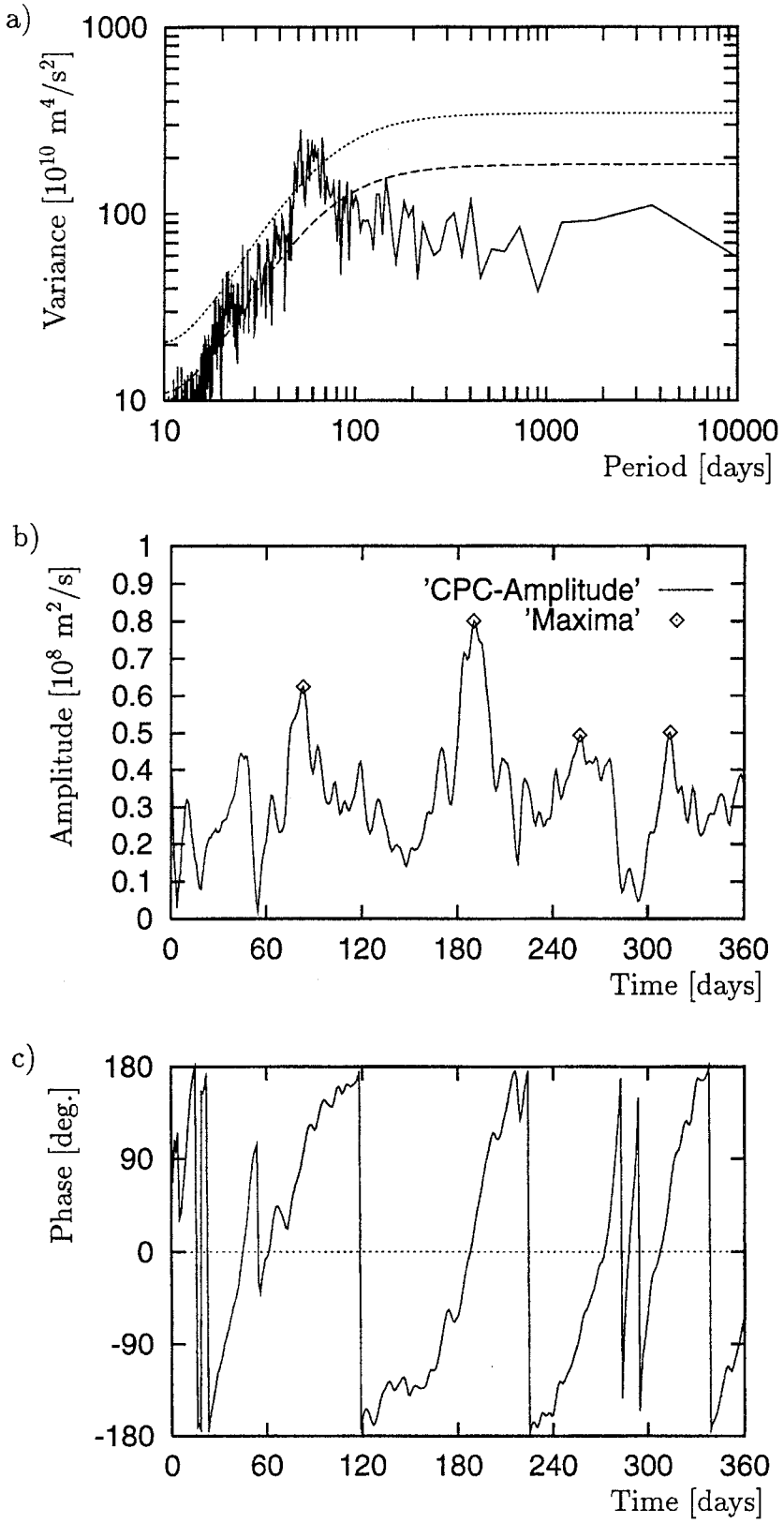

Figure 10. (a) The variance spectrum for the amplitude of CPC-1 (see text) with the spectrum of the equivalent red noise (dashed line); the dotted curve gives a 99% confidence limit for accepting a red-noise null hypothesis. Time-series samples of (b) the amplitude and (c) the phase of CPC-1. In (b) the maxima are identified for the subsequent composite analysis.

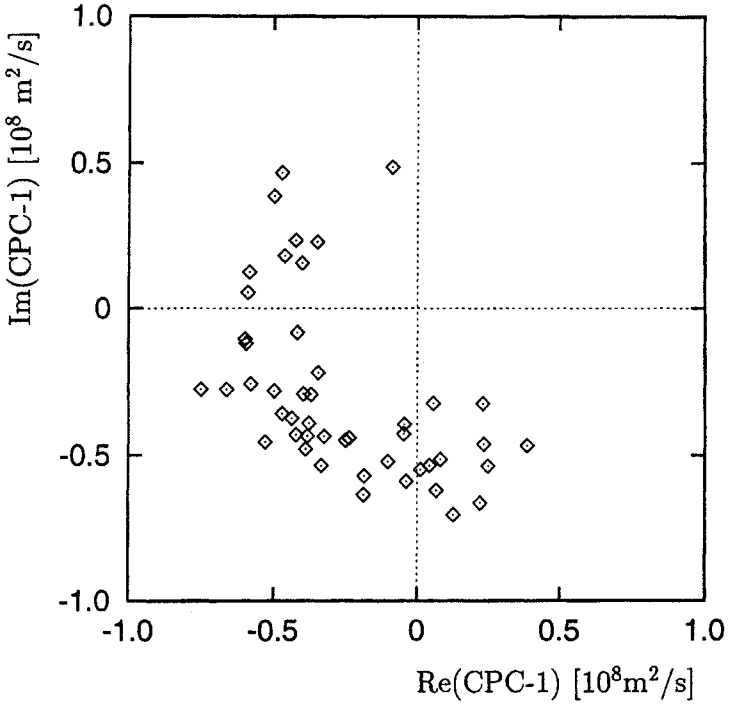

Figure 11. Scatter diagram for the maxima in the amplitude of CPC-1 (see text) in the complex plane.

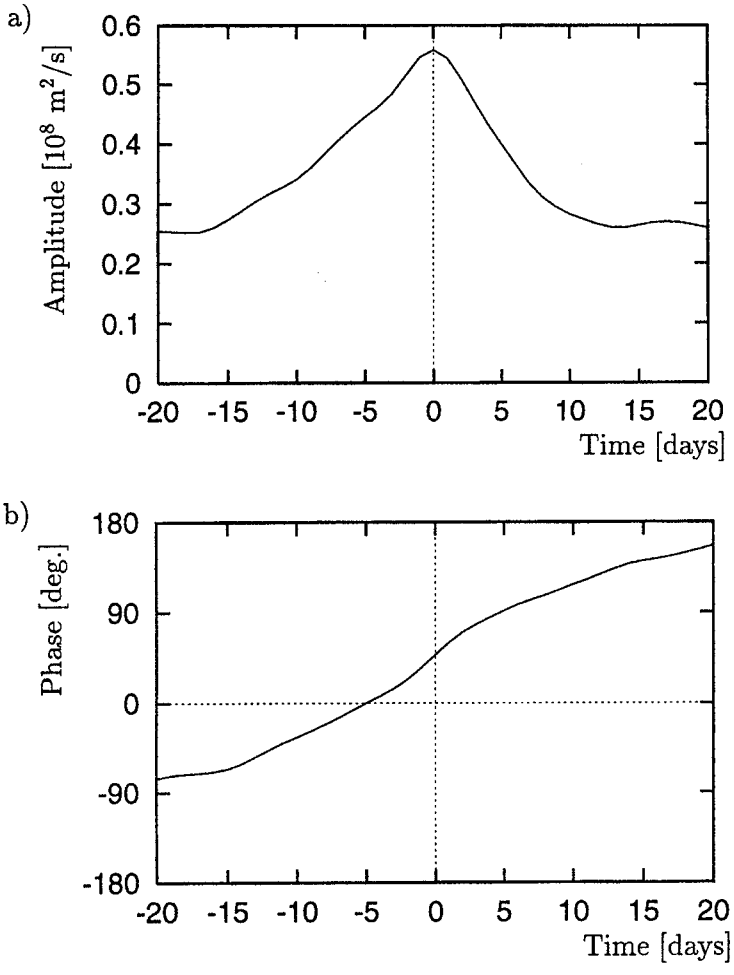

Figure 12. Composite evolution of (a) the amplitude and (b) the phase of CPC-1 (see text).

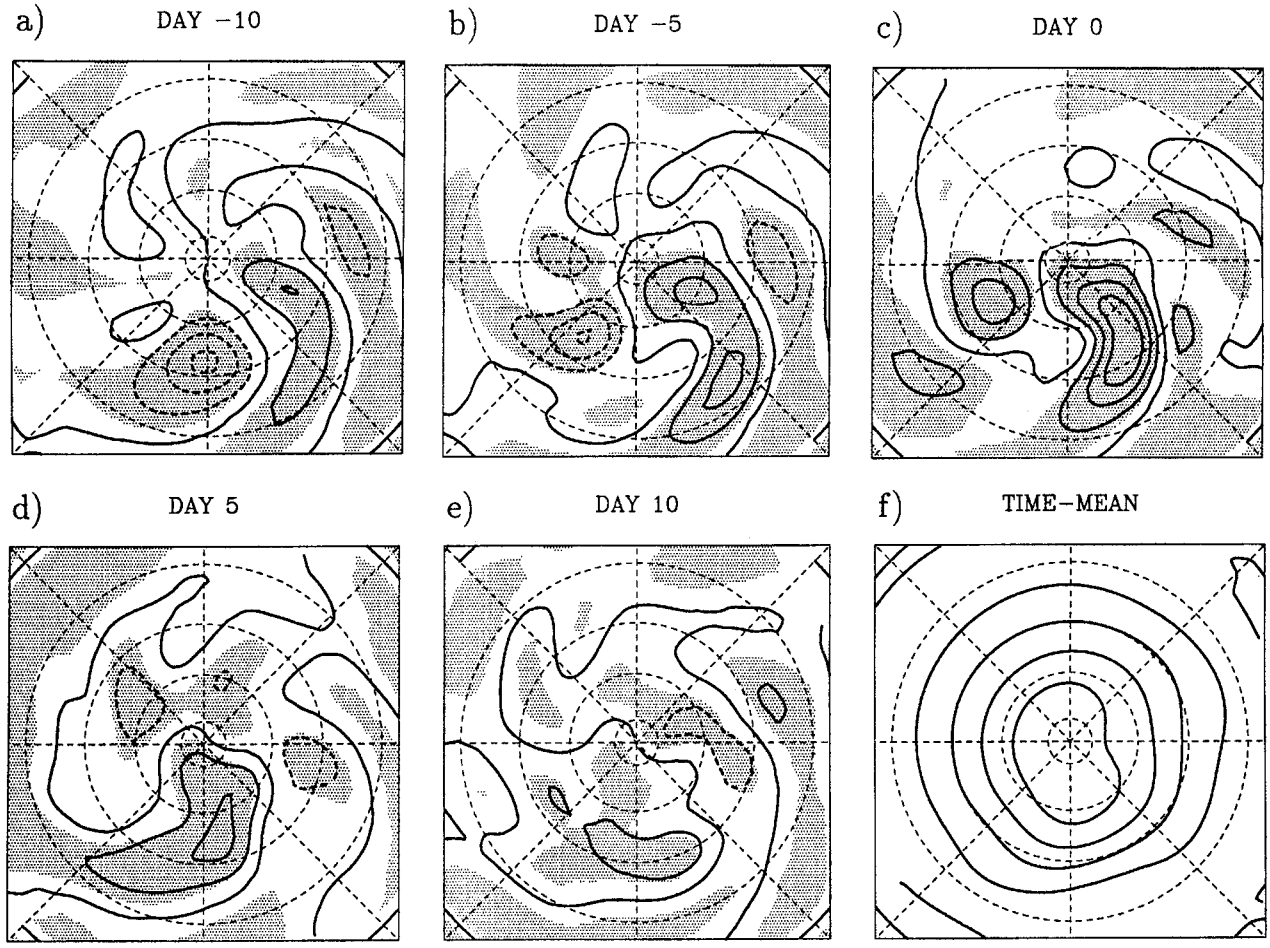

Figure 13. Composites at (a) day −10, (b) day −5, (c) day 0, (d) day 5, and (e) day 10 of the anomalous vertically averaged stream function. Contour interval is 0.02×10^8 m^{2}s^{-1} and negative isolines are dashed. The shading indicates the areas of statistical significance at the 99% level. (f) Vertically averaged time-mean stream function (contour interval 0.15×10^8 m^{2}s^{-1}).

(not shown) reveals an equivalent barotropic structure of the low-frequency anomaly with maximum amplitude at 500 hPa. In Fig. 14 the composites of the bandpass filtered standard deviation of 500 hPa geopotential height are displayed together with the $\hat{\psi}$-composites. One observes a considerable variability of the intensity and location of the storm track during the CPC-1 life cycle: the storm track is displaced and elongated in the zonal rather than in the meridional direction. Eddy activity decreases after the disturbance has passed the ridge (which also undergoes changes in position and amplitude). The largest amplitude of eddy activity is found at day 0. The composite evolution of the standard-deviation maximum (Fig. 15) shows cyclogenesis beginning at day −5 which seems to cause the peak in CPC-1 amplitude. However, this event cannot solely be responsible for the growth of the anticyclonic anomaly since this anomaly already exists before the cyclogenesis starts.

In order to gain insight into the underlying dynamical mechanism for the low-frequency anomaly, it is useful to discuss the feedback of the high-frequency eddies onto the quasi-stationary flow. This feedback can be determined by the forcing of the stream function, neglecting the vertical advection term (Hoskins *et al.* 1983)

$$S = -\nabla^{-2}\{\nabla \cdot (\mathbf{v}'\eta' + \bar{\mathbf{v}}\eta' + \mathbf{v}'\bar{\eta})\}. \tag{16}$$

Figure 16 shows the composites of the vertically averaged stream-function source anomaly $\hat{S}$ (climatology subtracted) where the eddies are computed from the bandpass filtered

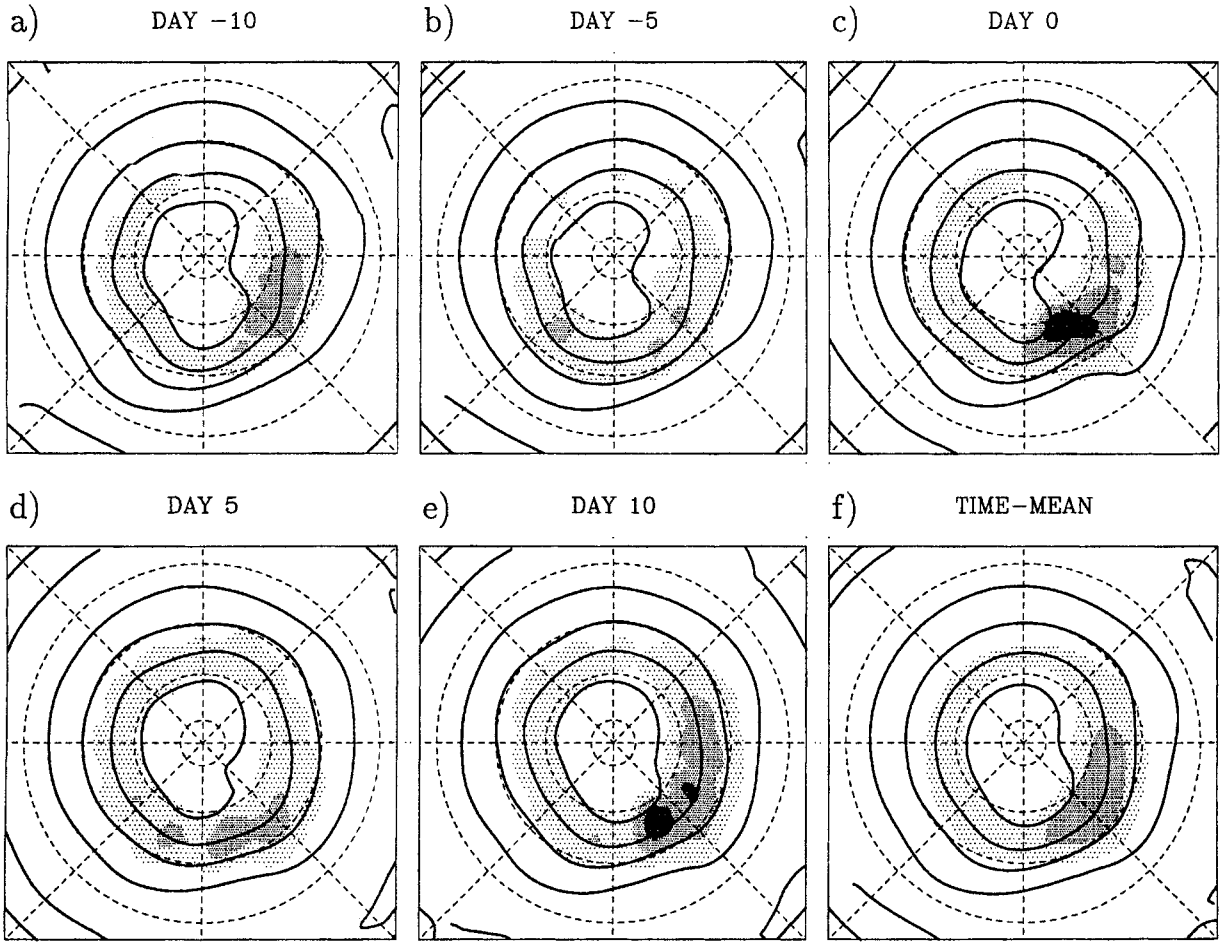

Figure 14. Composites at (a) day −10, (b) day −5, (c) day 0, (d) day 5, (e) day 10, and the time-mean (f) of the standard deviation of bandpass filtered 500 hPa height (stippling) and of the vertically averaged stream function. The values of the standard deviation falling within the ranges of 15–25, 25–35 and > 35 m are indicated by light, medium and dense stippling, respectively. The contour interval is 0.15×10^8 $m^2 s^{-1}$.

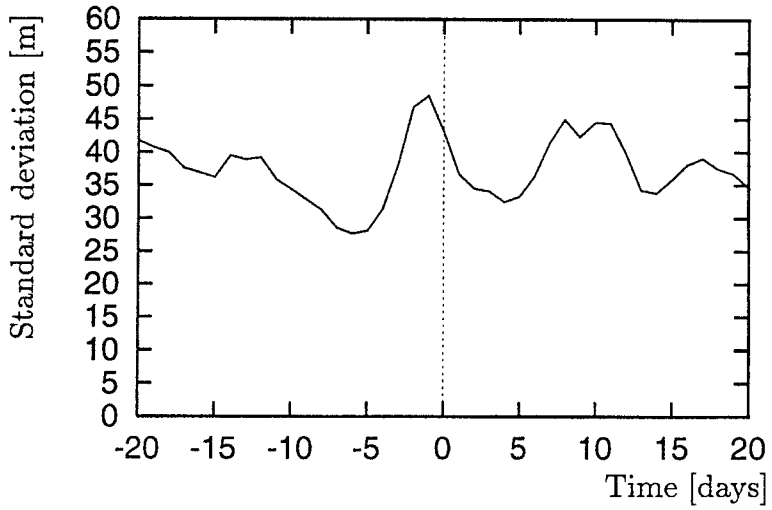

Figure 15. Composite evolution of the standard-deviation maximum of bandpass filtered 500 hPa height.

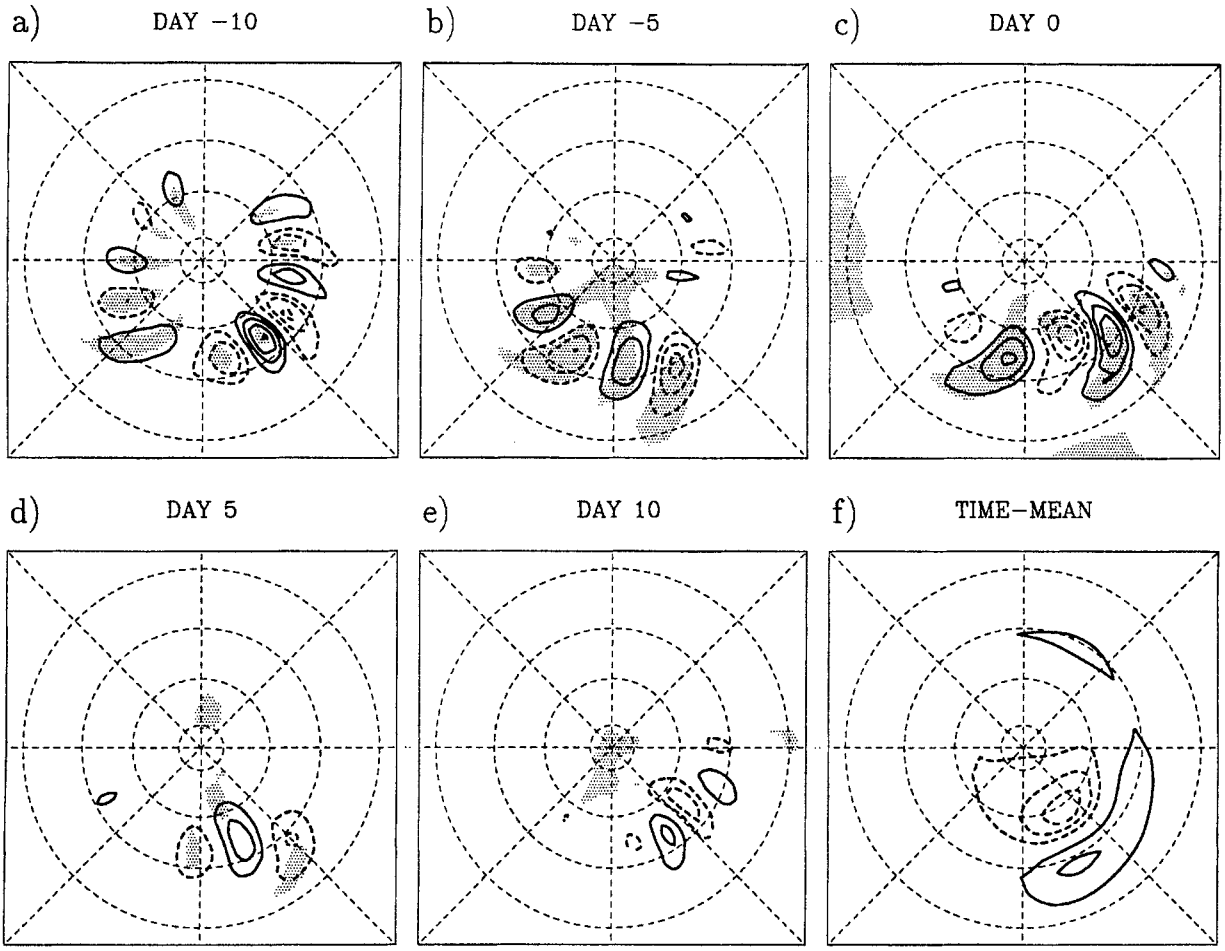

Figure 16. Composites at (a) day −10, (b) day −5, (c) day 0, (d) day 5 and (e) day 10 of the anomalous vertically averaged stream-function source calculated from bandpass filtered data. The shading indicates the areas of statistical significance at the 99% level. The contour interval is 5 m^2s^{-2}, negative isolines are dashed, and the zero line is not displayed. (f) Vertically averaged time-mean stream-function source calculated from bandpass filtered data (contour interval 2 m^2s^{-2}).

data: at the maximum in CPC-1 amplitude (day 0) the stream-function source exhibits a statistically significant single synoptic-scale wave pattern. It seems to develop from the significant wave pattern found upstream at day −5 and day −10. This surprising result indicates that the low-frequency anomaly is locked in phase with high-frequency eddies. Note that the last two terms in (16) which dominate the $\widehat{S}$ distribution vanish if time averaging is applied. A set of Hovmüller diagrams (along 52.6°N) comprises the analysis (Fig. 17):

(a) The composite of the vertically averaged unfiltered stream-function anomaly $\widehat{\psi}$ (Fig. 17(a)) shows the upstream propagating low-frequency wave with maximum amplitude near day 0.

(b) The life cycle of the anticyclonic anomaly is in good agreement with a stream-function anomaly (Fig. 17(b)) obtained from the accumulated stream-function source (that is the time integral of the vertically averaged source anomaly $\widehat{S}$ assuming $\widehat{S} = 0$ at day −25). The missing propagation can be explained by Rossby-wave dynamics of the planetary-scale anticyclone which is not captured by the bandpass filtered data.

(c) The composite of the bandpass filtered stream-function source $\widehat{S}$ itself (Fig. 17(c)) reveals the eastward propagation of the phase locked synoptic-scale wave which develops upstream of the heating dipole.

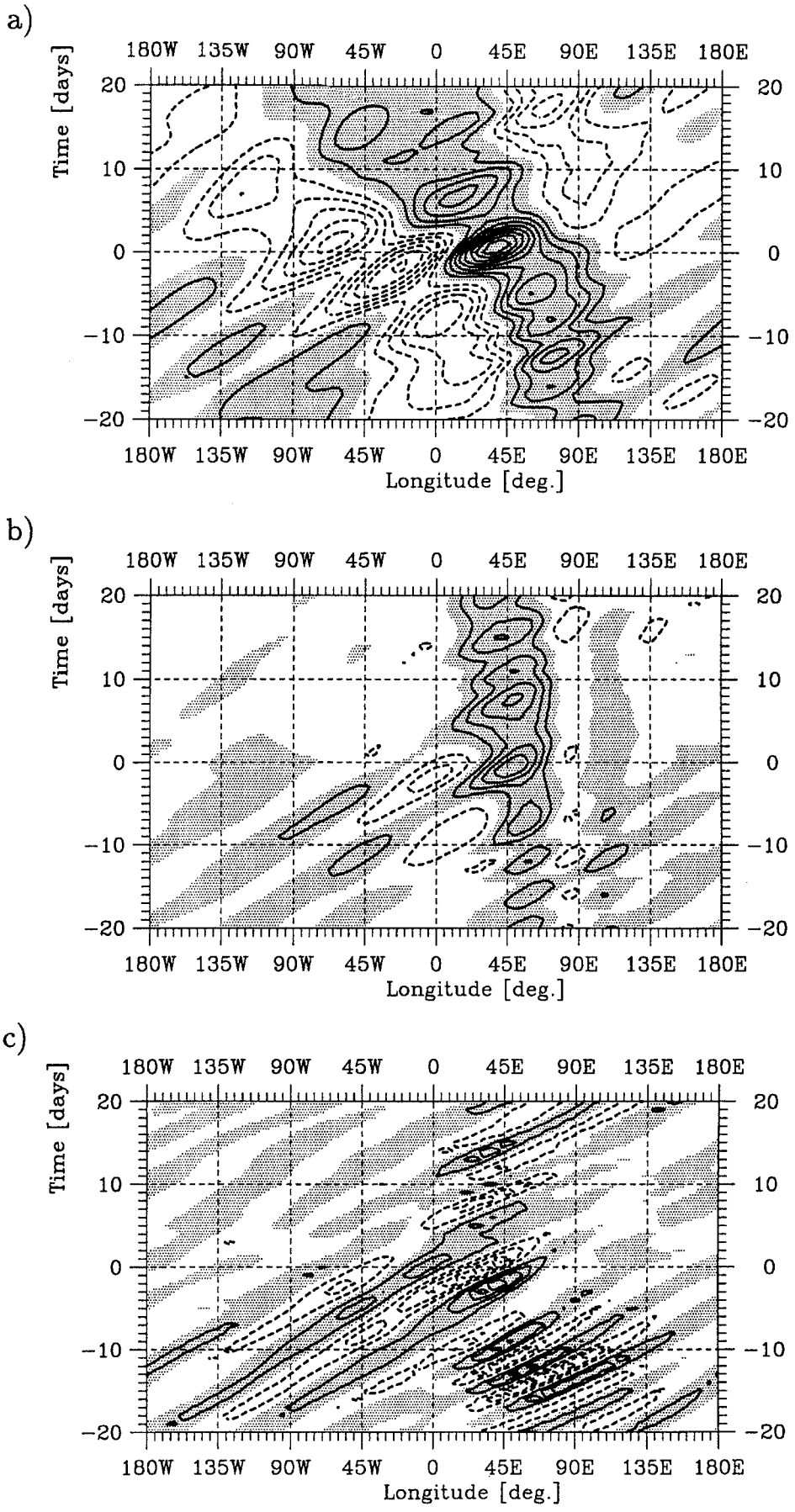

Figure 17. Hovmüller diagrams at 52.6°N of the composite of (a) anomalous vertically averaged stream function (contour interval 10^6 m^2s^{-1}), (b) the time integrated anomalous vertical averaged stream-function source calculated from bandpass filtered data (contour interval 10^6 m^2s^{-1}), and (c) the anomalous vertical averaged stream-function source calculated from bandpass filtered data (contour interval 5 m^2s^{-2}). Positive values are shaded and negative isolines are dashed.

5. Discussion and conclusions

The organization of a storm track has been examined in a simplified global atmospheric circulation model. A well established storm track can be simulated by a zonally asymmetric distribution of heating consisting of a dipole embedded in a zonally symmetric profile. Three simulations, each with a different dipole orientation, are performed to test the sensitivity of the storm-track organization to the shape of the heating distribution. They all show localization of the eddy energy.

The case with a north-east orientation (NE-case) of the isolines between the restoration temperature poles appears to be the most realistic one. In this case the simulated time-mean circulation and the distribution of the transient eddies are in good agreement with observations of the northern hemisphere wintertime storm tracks (Blackmon *et al.* 1977). The main difference from observations lies in the weak amount of eddy kinetic energy, resulting probably from the large damping in the Newtonian cooling formulation and the coarse resolution of the model. The strong zonal variation of baroclinicity and the distribution of the temperature fluxes suggest that local baroclinic instability is responsible for the localization of eddy kinetic energy. The zonal variation of baroclinicity is maintained mainly by the distribution of heating, consistent with the results of Hoskins and Valdes (1990).

The storm-track organization of the NE-case is investigated with local energetics. The local balance equation for transient kinetic energy contains four terms: advection, baroclinic production, shear production (destruction) and dissipation. The kinetic energy of the storm track is mainly generated by baroclinic production. Negative shear production (that is destruction of eddy energy) dominates the downstream end of the storm track, suggesting that the shear production is responsible for its location. This is in agreement with the results of Whittaker and Dole (1995), where the locus of the end of the storm track also results from the horizontal deformation of the eddies.

In comparison, Chang and Orlanski (1993) simulated a storm track without a clearly established downstream end which, as presumed by Whittaker and Dole (1995), might be a consequence of weak horizontal deformation of the eddies. That is, the simulation of a storm track is sensitive to the design of the experiment. In their experiments, Chang and Orlanski (1993) introduce a sponge region where strong Newtonian damping forces the flow towards a baroclinic state and eddies are efficiently damped out. Outside the sponge region no forcing is applied. In our experiments moderate Newtonian cooling and Rayleigh friction are applied globally. The reasonably good agreement of the simulated fields with observations justifies our experimental design even if the orography, condensational processes, and zonal variation of friction are neglected, which limits the comparison to the observed storm tracks.

Low-frequency variability is found in the simulation of the NE-case as well as the high-frequency eddies. It is described by the first complex EOF of the vertically averaged stream function. The largest variance of the CPC-1 amplitude occurs at a period of about 50 days; the phase of the CPC-1 indicates that the anomaly retrogrades. Such retrogressions of the low-frequency anomalies are also identified by Kushnir (1987) and Lanzante (1990) in the northern Pacific where maximum amplitude is observed over the Gulf of Alaska.

Details of the underlying mechanism are explored by composites of 47 maxima in the CPC-1 time series. The life cycle of the CPC-1 amplitude composite describes a blocking-like event; in most cases the maxima have phases with an anticyclonic anomaly in the eastern or downstream part of the storm track. In contrast, Kushnir (1987) shows the phases of the retrograding Pacific anomaly at the time of maximum amplitude to be randomly distributed. The composite life cycle of this retrograding anticyclonic anomaly

lasts about 40 days. The associated composites of the bandpass filtered standard deviation of 500 hPa height reveal substantial change of storm-track activity due to the low-frequency anomalies. The downstream end of the storm track coincides with the position of the stationary anticyclonic ridge. The storm track varies mainly in the zonal direction.

The relationship between the high-frequency eddies and the low-frequency fluctuations confirms the results of Lau's (1988) data analysis: the CEOF-1 pattern with the associated changes of eddy activity bears some analogy to his Pacific P3-mode, which shows that the Pacific storm track is accompanied by a downstream blocking ridge over the Aleutians (Alaska blocking). Furthermore, as the zonal displacement and the elongation of the simulated storm track dominates over changes in the meridional direction, there is more similarity with the characteristics of the observed North Pacific than the North Atlantic storm track.

A cyclogenesis event in the upstream storm track occurs a few days before the CPC-1 amplitude peak, which is in good agreement with synoptic case-studies of blocking events (Colucci 1985). A surprising result is the phase-locking of a high-frequency wave train with the CPC-1 life cycle. This wave train propagates around the globe, initiating the cyclogenesis in the upstream part of the storm track. Although the high-frequency transient eddies seem to force the blocking anticyclone, which agrees with the results of previous studies (Mullen 1987), they are not able to maintain this anomaly over a longer period. The contrast to the observed persistence of blocks lasting for about two weeks (Rex 1950) may possibly be related to the weakness of the simulated eddies and the exclusion of orography. Some studies (Frederiksen 1982; Simmons *et al.* 1983; Kushnir 1987) suggest that hydrodynamic instability of the time-mean flow is responsible for the excitation of low-frequency anomalies. However, hydrodynamic instability does not seem to be responsible for the low-frequency variability in the NE-case since the composite energy cycle of the low-pass filtered data (not shown) indicates no increased barotropic or baroclinic energy conversions during the growth of the blocking anticyclone.

Acknowledgements

The detailed and very helpful comments of the two referees are greatly appreciated. Financial support was provided by the Bundesministerium für Bildung, Wissenschaft, Forschung und Technologie (07VKV01/1), the ARC-project (313-ARC-IX-scu) and the European Community under contract EV5V-CT94-0503.

Appendix

Restoration-temperature field

The restoration-temperature field (target state) to which the temperature will be relaxed is prescribed by T_E. In order to simulate a storm track, the T_E distribution consists of a zonally varying temperature gradient. A temperature dipole is superimposed on a zonally symmetric temperature profile. The temperature T_E is written:

$$T_E(\lambda, \varphi, \sigma) = T_0(\sigma) + f(\sigma)\left[70\,\mathrm{K}\left(\frac{1}{3} - \sin^2\varphi\right)\right.$$
$$\left. -50\,\mathrm{K}\sum_{j=1}^{2}(-1)^j \exp\{-d_{\lambda j}\cos^2\varphi(\lambda-\lambda_j)^2 - d_{\varphi j}(\varphi-\varphi_j)^2\}\right], \quad \text{(A.1)}$$

where λ is the longitude, φ is the latitude, $T_0(\sigma)$ is a function describing the globally averaged vertical temperature structure with $T_0(1) = 288$ K. The index $j = 1, 2$ denotes the

TABLE A.1. VALUES OF THE PARAMETERS DESCRIBING THE RESTORATION TEMPERATURE

Parameter	NE-case	Z-case	SE-case
λ_1	0°E	0°E	0°E
λ_2	35°W	0°E	35°E
φ_1	40°N	31.8°N	40°N
φ_2	50°N	58.2°N	50°N
d_{λ_1} for $\lambda \geq \lambda_1$	5 rad^{-2}	5 rad^{-2}	9 rad^{-2}
d_{λ_1} for $\lambda < \lambda_1$	9 rad^{-2}	5 rad^{-2}	5 rad^{-2}
d_{λ_2} for $\lambda \geq \lambda_2$	9 rad^{-2}	5 rad^{-2}	5 rad^{-2}
d_{λ_2} for $\lambda < \lambda_2$	5 rad^{-2}	5 rad^{-2}	9 rad^{-2}
d_{φ_1} for $\varphi \geq \varphi_1$	10 rad^{-2}	10 rad^{-2}	10 rad^{-2}
d_{φ_1} for $\varphi < \varphi_1$	20 rad^{-2}	20 rad^{-2}	20 rad^{-2}
d_{φ_2} for $\varphi \geq \varphi_2$	20 rad^{-2}	20 rad^{-2}	20 rad^{-2}
d_{φ_2} for $\varphi < \varphi_2$	10 rad^{-2}	10 rad^{-2}	10 rad^{-2}

For explanation of symbols and headings see text.

warm and cold spot, respectively, and the function $f(\sigma)$ describes the vertical dependence of the temperature anomaly:

$$f(\sigma) = \begin{cases} \sin\left(\frac{\pi}{2}\frac{\sigma - 0.19}{1 - 0.19}\right) & \text{for } \sigma \geq 0.19 \\ 0 & \text{for } \sigma < 0.19. \end{cases} \tag{A.2}$$

The temperature gradients decrease monotonically with height and vanish above the tropopause at $\sigma = 0.19$. The parameters describing the structure of the temperature dipole of the three experiments are given in Table A.1.

REFERENCES

Blackmon, M. L. 1976 A climatological spectral study of the 500 mb geopotential height of the northern hemisphere. *J. Atmos. Sci.*, **33,** 1607–1623

Blackmon, M. L., Wallace, J. M., Lau, N. C. and Mullen, S. L. 1977 An observational study of the northern hemisphere wintertime circulation. *J. Atmos. Sci.*, **34,** 1040–1053

Chang, E. K. M. and Orlanski, I. 1993 On the dynamics of a storm track. *J. Atmos. Sci.*, **50,** 999–1015

Colucci, S. J. 1985 Explosive cyclogenesis and large-scale circulation changes: Implications for atmospheric blocking. *J. Atmos. Sci.*, **42,** 2701–2717

Dole, R. M. 1986 The life cycles of persistent anomalies and blocking over the North Pacific. *Adv. Geophys.*, **29,** 31–69, Academic Press

Eady, E. T. 1949 Long waves and cyclone waves. *Tellus*, **1,** 33–52

Frederiksen, J. S. 1982 A unified three-dimensional instability theory of the onset of blocking and cyclogenesis. *J. Atmos. Sci.*, **39,** 969–982

1983 Disturbances and eddy fluxes in northern hemisphere flows: Instability of three-dimensional January and July flows. *J. Atmos. Sci.*, **40,** 836–855

Hall, N. M. J., Hoskins, B. J., Valdes, P. J. and Senior, C. A. 1994 Storm tracks in a high-resolution GCM with doubled carbon dioxide. *Q. J. R. Meteorol. Soc.*, **120,** 1209–1230

Held, I. M. 1983 'Stationary and quasi-stationary eddies in the extratropical troposphere: Theory'. Pp. 127–168 in *Large-scale dynamical processes in the atmosphere*. Eds. B. J. Hoskins and R. P. Pearce. Academic Press

Held, I. M. and Suarez, M. J. 1994 A proposal for the intercomparison of the dynamical cores of atmospheric general circulation models. *Bull. Am. Meteorol. Soc.*, **75,** 1825–1830

Horel, J. D.	1984	Complex principal component analysis: Theory and examples. *J. Clim. Appl. Meteorol.*, **23,** 1660–1673
Hoskins, B. J. and Simmons, A. J.	1975	A multi-layer spectral model and the semi-implicit method. *Q. J. R. Meteorol. Soc.*, **101,** 637–655
Hoskins, B. J. and Valdes, P. J.	1990	On the existence of storm tracks. *J. Atmos. Sci.*, **47,** 1854–1864
Hoskins, B. J., James, I. N. and White, G. H.	1983	The shape, propagation and mean-flow interaction of large-scale weather systems. *J. Atmos. Sci.*, **40,** 1595–1612
Illari, L. and Marshall, J. C.	1983	On the interpretation of eddy fluxes during a blocking episode. *J. Atmos. Sci.*, **40,** 2232–2242
James, I. N.	1994	*Introduction to circulating atmospheres*. Cambridge University Press, Cambridge, UK
James, I. N. and Gray, L. J.	1986	Concerning the effect of surface drag on the circulation of a baroclinic planetary atmosphere. *Q. J. R. Meteorol. Soc.*, **112,** 1231–1250
James, I. N. and James, P. M.	1992	Spatial structure of ultra-low-frequency variability of the flow in a simple atmospheric circulation model. *Q. J. R. Meteorol. Soc.*, **118,** 1211–1233
James, P. M., Fraedrich, K. and James, I. N.	1994	Wave–zonal-flow interaction and ultra-low-frequency variability in a simplified global circulation model. *Q. J. R. Meteorol. Soc.*, **120,** 1045–1067
Kushnir, Y.	1987	Retrograding wintertime low-frequency disturbances over the North Pacific Ocean. *J. Atmos. Sci.*, **44,** 2727–2742
Lanzante, J. R.	1990	The leading modes of 10–30 day variability in the extratropics of the northern hemisphere during the cold season. *J. Atmos. Sci.*, **47,** 2115–2140
Lau, N.-C.	1979a	The structure and energetics of transient disturbances in the northern hemisphere wintertime circulation. *J. Atmos. Sci.*, **36,** 982–995
	1979b	The observed structure of tropospheric stationary waves and the local balances of vorticity and heat. *J. Atmos. Sci.*, **36,** 996–1016
	1988	Variability of the observed midlatitude storm tracks in relation to low-frequency changes in the circulation pattern. *J. Atmos. Sci.*, **45,** 2718–2743
Lindzen, R. S. and Farrell, B.	1980	A simple approximate result for the maximum growth rate of baroclinic instabilities. *J. Atmos. Sci.*, **37,** 1648–1654
Lorenz, E. N.	1955	Available potential energy and the maintenance of the general circulation. *Tellus*, **7,** 157–167
Lunkeit, F., Ponater, M., Sausen, R., Sogalla, M., Ulbrich, U. and Windelband, M.	1996	Cyclonic activity in a warmer climate. *Beitr. Phys. Atmos.*, **69,** 393–407
MacVean, M. K.	1983	The effects of horizontal diffusion on baroclinic development in a spectral model. *Q. J. R. Meteorol. Soc.*, **109,** 771–783
Mole, N. and James, I. N.	1990	Baroclinic adjustment in a zonally varying flow. *Q. J. R. Meteorol. Soc.*, **116,** 247–268
Mullen, S. L.	1987	Transient eddy forcing of blocking flows. *J. Atmos. Sci.*, **44,** 3–22
Nakamura, H. and Wallace, J. M.	1990	Observed changes in baroclinic wave activity during the life cycles of low-frequency circulation anomalies. *J. Atmos. Sci.*, **47,** 1100–1116
Pierrehumbert, R. T.	1984	Local and global baroclinic instability of zonally varying flow. *J. Atmos. Sci.*, **41,** 2141–2162
Rex, D. F.	1950	Blocking action in the middle troposphere and its effect upon regional climate. II: The climatology of blocking action. *Tellus*, **2,** 275–301
Simmons, A. J. and Hoskins, B. J.	1978	The life cycles of some nonlinear baroclinic waves. *J. Atmos. Sci.*, **35,** 414–432
Simmons, A. J., Wallace, J. M. and Branstator, G. W.	1983	Barotropic wave propagation and instability, and atmospheric teleconnection patterns. *J. Atmos. Sci.*, **40,** 1363–1392
Smagorinsky, J.	1953	The dynamical influence of large-scale heat sources and sinks on the quasi-stationary mean motions of the atmosphere. *Q. J. R. Meteorol. Soc.*, **79,** 342–366
Stephenson, D. B.	1994	The northern hemisphere tropospheric response to changes in the gravity-wave drag scheme in a perpetual January GCM. *Q. J. R. Meteorol. Soc.*, **120,** 699–712
Ting, M.	1994	Maintenance of northern summer stationary waves in a GCM. *J. Atmos. Sci.*, **51,** 3286–3308

Trenberth, K. E. 1991 Storm tracks in the southern hemisphere. *J. Atmos. Sci.*, **48,** 2159–2178

Valdes, P. J. and Hoskins, B. J. 1989 Linear stationary wave simulations of the time-mean climatological flow. *J. Atmos. Sci.*, **46,** 2509–2527

Wallace, J. M. and Gutzler, D. S. 1981 Teleconnections in the geopotential height field during the northern hemisphere winter. *Mon. Weather Rev.*, **109,** 784–812

Whittaker, J. S. and Dole, R. M. 1995 Organization of storm tracks in zonally varying flows. *J. Atmos. Sci.*, **52,** 1178–1191